


Crossover from itinerant to localized states in the thermoelectric oxide $[\text{Ca}_2\text{CoO}_3]_{0.62}[\text{CoO}_2]$ H. Sakabayashi and R. Okazaki *Department of Physics, Faculty of Science and Technology, Tokyo University of Science, Noda 278-8510, Japan*

(Received 29 December 2020; accepted 25 February 2021; published 8 March 2021)

The layered cobaltite $[\text{Ca}_2\text{CoO}_3]_{0.62}[\text{CoO}_2]$, often expressed as the approximate formula $\text{Ca}_3\text{Co}_4\text{O}_9$, is a promising candidate for efficient oxide thermoelectrics, but an origin of its unusual thermoelectric transport is still in debate. Here we investigate in-plane anisotropy of the transport properties in a broad temperature range to examine the detailed conduction mechanism. The in-plane anisotropy between a and b axes is clearly observed both in the resistivity and the thermopower, which is qualitatively understood with a simple band structure of the triangular lattice of Co ions derived from the angle-resolved photoemission spectroscopy experiments. On the other hand, at high temperatures the anisotropy becomes smaller and the resistivity shows a temperature-independent behavior, both of which indicate a hopping conduction of localized carriers. Thus, the present observations reveal a crossover from low-temperature itinerant to high-temperature localized states, signifying both characters for the enhanced thermopower.

DOI: [10.1103/PhysRevB.103.125119](https://doi.org/10.1103/PhysRevB.103.125119)

I. INTRODUCTION

The layered cobaltites provide a fascinating platform for exploring functional properties of oxides both in fundamental and applicational viewpoints [1]. Since the discovery of large thermopower in the metallic Na_xCoO_2 [2], this class of materials has been recognized as potential oxide thermoelectrics that possess a high-temperature stability in air [3–5]. The crystal structure of this family is composed of two subsystems of an insulating layer and a CdI_2 -type CoO_2 conduction layer, alternately stacked along the c axis. As for the origin of the large thermopower coexisting with the metallic conductivity, Koshibae *et al.* have suggested a localized model in which a hopping conduction of correlated d electrons with spin and orbital degeneracies involves large entropy flow [6]. This picture is supported by magnetic field dependence of the thermopower [7] and is also discussed in semiconducting cobalt oxides [8]. On the other hand, Kuroki *et al.* have proposed an itinerant model based on “pudding-mold” band structure, in which the difference in velocities of electrons and holes is crucial [9]. Indeed, such a peculiar band shape is observed by angle-resolved photoemission spectroscopy (ARPES) experiments [10–14] and a large value of thermopower is calculated accordingly [15,16]. The detailed conduction mechanism in this system remains controversial.

The misfit oxide $[\text{Ca}_2\text{CoO}_3]_{0.62}[\text{CoO}_2]$ [17–19] is a suitable compound to shed light on the above fundamental issue, because it straddles a border between localized and itinerant states of Co $3d$ electrons, from which interesting emergent phenomena appear in correlated electron systems [20]. As shown in Figs. 1(a) and 1(b), this material has a rocksalt-type Ca_2CoO_3 block as an insulating layer, and its b -axis lattice parameter b_2 is different from that of CoO_2 layer b_1 , leading to a misfit structure with incommensurate ratio of $b_1/b_2 \simeq 0.62$. This system is often referred as the approx-

imate formula $\text{Ca}_3\text{Co}_4\text{O}_9$. The metallic transport properties, along with a spin-density-wave (SDW) formation at $T_{\text{SDW}} \simeq 30$ K [22–24], indicate an itinerant nature, although the magnetic structure revealed by recent neutron experiments is quite unconventional [25]. On the other hand, compared with that of Na_xCoO_2 , this compound has moderately high resistivity [26], which is close to the Ioffe-Regel limit [18]. Negative magnetothermopower is also found in $[\text{Ca}_2\text{CoO}_3]_{0.62}[\text{CoO}_2]$ [27]. In addition, large thermopower of $Q \simeq 130 \mu\text{V/K}$ near room temperature is well explained in the extended Heikes formula based on the localized hopping picture of correlated electrons [28], which reveals not only in the conduction layer but also the rocksalt one as suggested by recent spectroscopic studies [29]. These experimental facts imply a complicated coexistence of itinerant and localized natures in this compound.

In this study, we argue the itinerancy and localization of conduction electrons in $[\text{Ca}_2\text{CoO}_3]_{0.62}[\text{CoO}_2]$ by means of in-plane transport anisotropy measurements between a - and b -axis directions. This is less investigated so far compared to the strong anisotropy between in-plane and out-of-plane directions [18,30], but is essential for thorough understanding of the underlying conduction mechanism. We find a considerable temperature dependence of the in-plane anisotropy both in resistivity and thermopower. Below room temperature, the in-plane anisotropy is relatively large and qualitatively explained by the anisotropy of the electronic velocities near the Fermi energy estimated from the results of ARPES experiments [31]. This is also consistent with the results of recent band calculation [32], indicating the itinerant nature in this system. Near $T_{\text{SDW}} \simeq 30$ K, the in-plane anisotropy drastically varies, possibly due to a reconstruction of the Fermi surface. Above room temperature, in contrast, we find that the in-plane anisotropy is close to unity as temperature increases, which is captured as a localized picture. The present results unveil

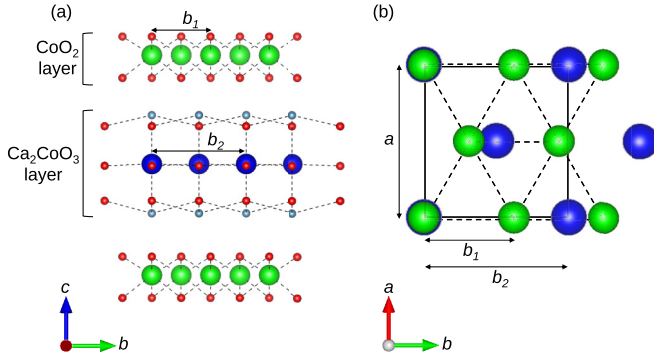


FIG. 1. Schematic view of the crystal structure of layered $[\text{Ca}_2\text{CoO}_3]_{0.62}[\text{CoO}_2]$ projected from (a) a axis and (b) c axis drawn by VESTA [21]. While the a -axis lattice parameter a is common, the b -axis lattice parameter of the rocksalt layer b_2 is different from that of CoO_2 layer b_1 , resulting in a misfit structure with incommensurate ratio of $b_1/b_2 \simeq 0.62$. The Co ions in CoO_2 (green) and rocksalt (blue) layers are shown in different colors for clarity.

the temperature-induced crossover from itinerant to localized states in $[\text{Ca}_2\text{CoO}_3]_{0.62}[\text{CoO}_2]$.

II. EXPERIMENTS

Single crystals of $[\text{Ca}_2\text{CoO}_3]_{0.62}[\text{CoO}_2]$ were grown by a flux method [33]. Powders of CaCO_3 (99.9%) and Co_3O_4 (99.9%) were mixed in a stoichiometric ratio and calcined two times in air at 1173 K for 20 h with intermediate grindings. Then KCl (99.999%) and K_2CO_3 (99.999%) powders mixed with a molar ratio of 1:4 was added with the calcined powder as a flux. The concentration of $[\text{Ca}_2\text{CoO}_3]_{0.62}[\text{CoO}_2]$ was set to be 1.5% in molar ratio. The mixture was put in an alumina crucible and heated up to 1123 K in air with a heating rate of 200 K/h. After keeping 1123 K for 1 h, it was slowly cooled down with a rate of 1 K/h, and at 1023 K the power of the furnace was switched off. As-grown samples were rinsed in distilled water to remove the flux and then annealed in air at 573 K for 3 h.

The typical dimension of obtained single crystals is $\simeq 4 \times 4 \times 0.01 \text{ mm}^3$ as shown in Fig. 2(a). The crystal orientation was determined by the Laue method. Although the spot intensity is weak in such thin samples, threefold symmetry from CoO_2 layer and fourfold symmetry from the rocksalt layer are resolved in the Laue pattern shown in Fig. 2(b). To discuss the anisotropy precisely, we cut one single crystal into two samples with the same rectangular shape of $\simeq 1 \times 0.3 \text{ mm}^2$ for the transport measurements along the a and b axes, as shown in Fig. 2(c). This method enables us to compare the transport properties of the samples with the same oxygen content. Note that the resistivity anisotropy was also checked by utilizing the Montgomery method near room temperature [34], although it may produce a fairly large systematic error bar [35]. The sample thickness of $\simeq 5 \text{ }\mu\text{m}$ was determined by the scanning electron microscopy (SEM) as shown in Fig. 2(d). The resistivity and the thermopower were simultaneously measured by using a conventional four-probe method and a steady-state method, respectively. The thermoelectric voltage from the wire leads was carefully subtracted. We used

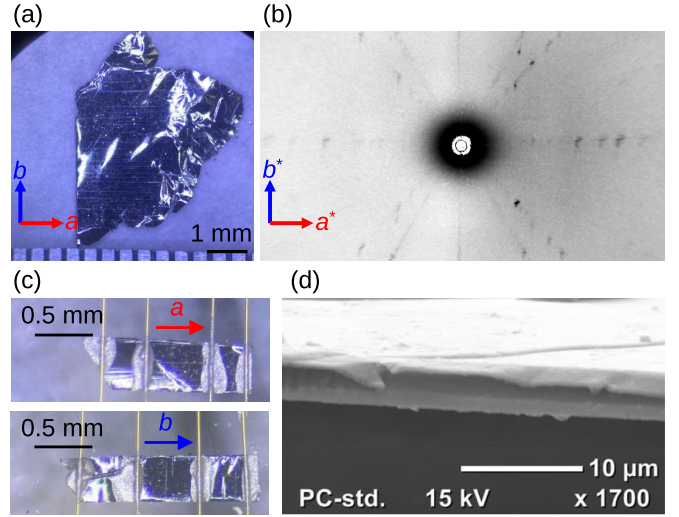


FIG. 2. (a) Photograph of a single crystal of $[\text{Ca}_2\text{CoO}_3]_{0.62}[\text{CoO}_2]$ and (b) Laue pattern. (c) Photographs of samples for the resistivity measurements. Two samples with the rectangular shape of $\sim 1 \times 0.3 \text{ mm}^2$ were obtained by cutting one single crystal. (d) SEM image of $[\text{Ca}_2\text{CoO}_3]_{0.62}[\text{CoO}_2]$ for the sample thickness measurement.

a Gifford-McMahon refrigerator below room temperature and an electrical furnace for high-temperature measurement.

III. RESULTS AND DISCUSSION

A. Temperature variations of resistivity and thermopower

Figure 3 summarizes the temperature variations of the in-plane transport properties in $[\text{Ca}_2\text{CoO}_3]_{0.62}[\text{CoO}_2]$. Hereafter we use an abbreviated form like $\rho_a (= \rho_{aa})$ for the resistivity measured along the a -axis direction. Overall behaviors are well reproduced compared with the earlier reports in which the transport coefficients are measured with no distinction among the in-plane directions [18]. In addition, the thermopower measured along the b axis Q_b is larger than that along the a axis Q_a , consistent with recent theoretical calculation [32]. At low temperature, below $\sim 100 \text{ K}$, the resistivity shows an insulating behavior while the thermopower seems to be metallic, which is discussed in terms of carrier localization [36], pseudogap opening [37], or quantum criticality [38]. Near room temperature, the thermopower shows a temperature-independent behavior with a relatively large value of $Q \simeq 130 \text{ }\mu\text{V/K}$, quantitatively explained by the extended Heikes formula of

$$Q = -\frac{k_B}{e} \ln \left(\frac{g_3}{g_4} \frac{y}{1-y} \right), \quad (1)$$

where k_B is the Boltzmann coefficient, e the elementary charge, g_3 and g_4 the spin and orbital degeneracies of Co^{3+} and Co^{4+} ions, respectively, and y the Co^{4+} (hole) concentration [6]. Enhancement of the thermopower above room temperature possibly may be attributed to a small spin-state change near $T \simeq 380 \text{ K}$ [39], above which the degeneracy ratio g_3/g_4 may vary with temperature. At this temperature, a small anomaly has been observed in several quantities such as the resistivity, magnetic susceptibility, heat capacity, and

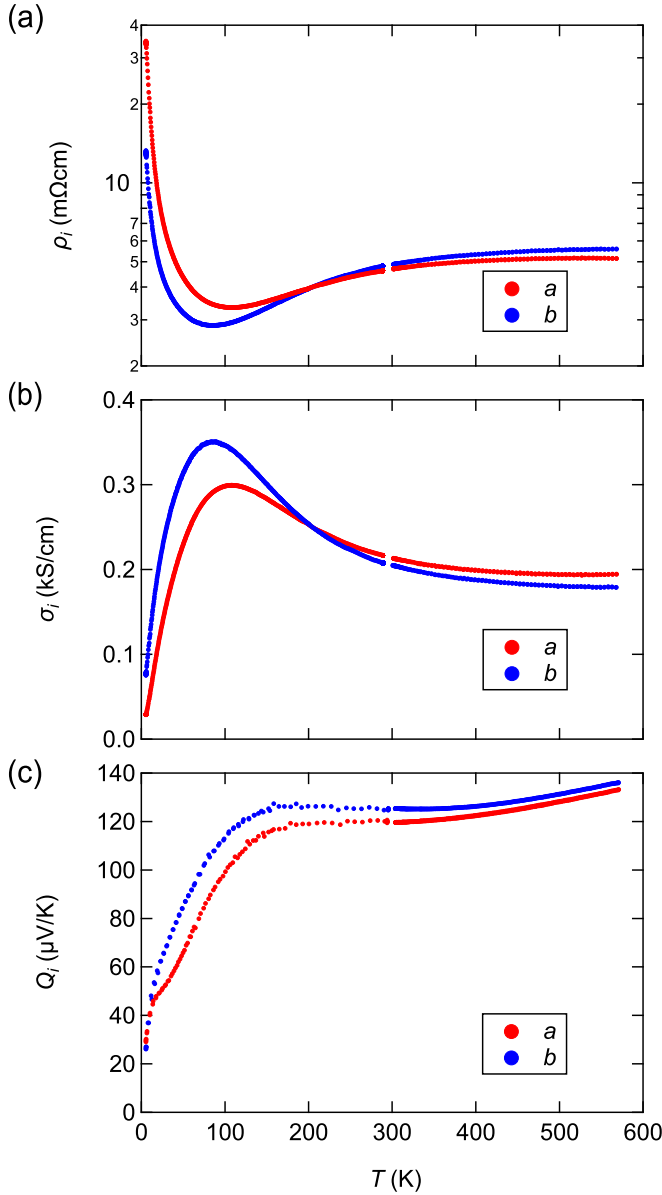


FIG. 3. Temperature variations of (a) resistivity ρ_i ($i = a, b$), (b) conductivity $\sigma_i = \rho_i^{-1}$, and (c) thermopower Q_i measured along the a - (red) and b -axis (blue) directions in $[\text{Ca}_2\text{CoO}_3]_{0.62}[\text{CoO}_2]$.

lattice constants [18,22,39]. On the other hand, the magnitude of the resistive anomaly may be sample-dependent [40] and is not resolved in the present samples. Although the present measurements are limited below 600 K, the increase of thermopower may continue up to 1000 K according to high-temperature transport experiments in this compound [41].

B. Localized state at high temperatures

We first discuss high-temperature transport. The inset of Fig. 4(a) shows the temperature dependence of the anisotropy of thermopower Q_b/Q_a . The anisotropy Q_b/Q_a decreases with increasing temperature and becomes close to unity near 600 K. This behavior is consistent with the localized model, because the thermopower at high temperatures can be

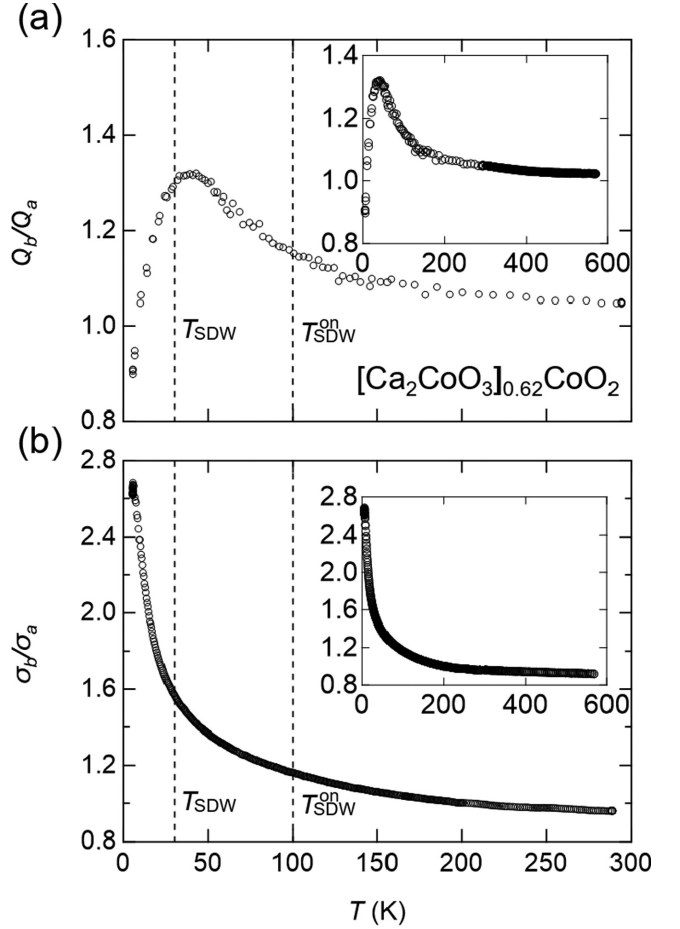


FIG. 4. Temperature variations of the transport anisotropy in (a) thermopower Q_b/Q_a and (b) electrical conductivity σ_b/σ_a below room temperature. The SDW transition temperature $T_{\text{SDW}} \simeq 30$ K and its onset $T_{\text{SDW}}^{\text{onset}} \simeq 100$ K are indicated by the dashed lines. The insets depict these anisotropies in the whole temperature range measured in the present study.

expressed by using chemical potential μ as

$$Q = -\frac{\mu}{eT}, \quad (2)$$

which leads to the Heikes formula of Eq. (1) [6], and the chemical potential in the numerator is a thermodynamic quantity, which does not give the anisotropic property. Note that other parameters to produce the anisotropy such as velocity and relaxation time are canceled out in Eq. (2). Therefore, the thermopower anisotropy, which should be unity within the Heikes formula, is an indicator for the localized electronic state.

Moreover, as shown in Fig. 3(a), the resistivity becomes less temperature-dependent in both directions at high temperatures. Such a behavior has also been observed in a high-temperature transport study while the in-plane orientation is undetermined [41], and is described as the hopping conduction at the Ioffe-Regel limit [42–44], at which the Fermi wavelength $\lambda_F (= 2\pi/k_F)$ (k_F being Fermi wavenumber) is comparable to the mean free path l of conduction electrons. Indeed, the dimensionless value of $k_F l$ estimated

from

$$k_F l = \frac{2\pi \hbar c_0}{e^2 \rho}, \quad (3)$$

where \hbar is the reduced Planck constant and c_0 is the c -axis length [37], is calculated as $k_F l \sim 0.54$ for the a -axis direction and 0.50 for the b -axis direction. Although there is an unavoidable error bar mainly due to the sample thickness, these values are close to unity, indicating the hopping conduction. Thus, these transport coefficients indicate the localized nature at high temperatures.

C. Itinerant state at low temperatures

We now focus on low-temperature transport anisotropy below room temperature. The main panels of Figs. 4(a) and 4(b) show the temperature variations of the anisotropies of thermopower Q_b/Q_a and electrical conductivity σ_b/σ_a below room temperature, respectively. In the temperature range of $40 \text{ K} \lesssim T \lesssim 300 \text{ K}$, both Q_b/Q_a and σ_b/σ_a increase with lowering temperature. Note that similar behaviors in thermopower and conductivity are also observed in the related layered cobaltite $(\text{Bi,Pb})_2\text{Sr}_2\text{Co}_2\text{O}_y$ [45], implying a universal anisotropic property in the CoO_2 -based materials, as is discussed below.

To clarify the origin of the anisotropic transport at low temperatures, we discuss the electronic band structure measured by ARPES at $T = 40 \text{ K}$ [31]. Note that the band structure is also proposed theoretically, but there is a difficulty originating from the misfit structure of this system in which an approximate formula is required for calculations [32,46–49]. In fact, the calculated thermopower strongly depends on the calculation methods [32,49]. Thus, the present results may offer an experimental clue for the challenging issue of theoretically obtaining the transport properties precisely in correlated electron systems with an incommensurate structure like this material. Now the band structure experimentally obtained in $[\text{Ca}_2\text{CoO}_3]_{0.62}[\text{CoO}_2]$ is well fitted by a tight-binding dispersion relation for the hexagonal lattice with primitive vectors \vec{a}_h and \vec{b}_h as [50]

$$\varepsilon(\mathbf{k}) = \varepsilon_0 - 2t \left\{ \cos(k_a a_h) + 2 \cos\left(\frac{\sqrt{3}}{2} k_b a_h\right) \cos\left(\frac{k_a a_h}{2}\right) \right\} - 2t' \{ \cos(2k_a a_h) + 2 \cos(\sqrt{3} k_b a_h) \cos(k_a a_h) \}, \quad (4)$$

where $\varepsilon_0 = -72.6 \text{ meV}$ is a constant and $a_h = 2.82 \text{ \AA}$ is the lattice constant. In this model, only the conducting CoO_2 layer is considered and modeled as a hexagonal lattice. $t = -25.4 \text{ meV}$ and $t' = 7.2 \text{ meV}$ denote the transfer integrals between atomic orbitals connected with \vec{a}_h and $2\vec{a}_h$. As is discussed in Ref. [31], tight-binding fit with t'' , which is transfer integral along the $\vec{a}_h + \vec{b}_h$ direction, leads to a wrong result, probably due to a one-dimensional σ -bond formation along the \vec{a}_h direction. Figure 5(a) shows the calculated contour plot for the constant-energy surfaces, in which a Fermi surface with a hexagonal shape is confirmed as seen in ARPES experiments [31]. Note that k_a and k_b directions correspond to $\sim a$ and b directions in real space, respectively [51].

Figure 5(b) shows the dispersion relations along the $\Gamma \rightarrow \text{K}$ and $\Gamma \rightarrow \text{M}$ directions. The flat region in the top of these

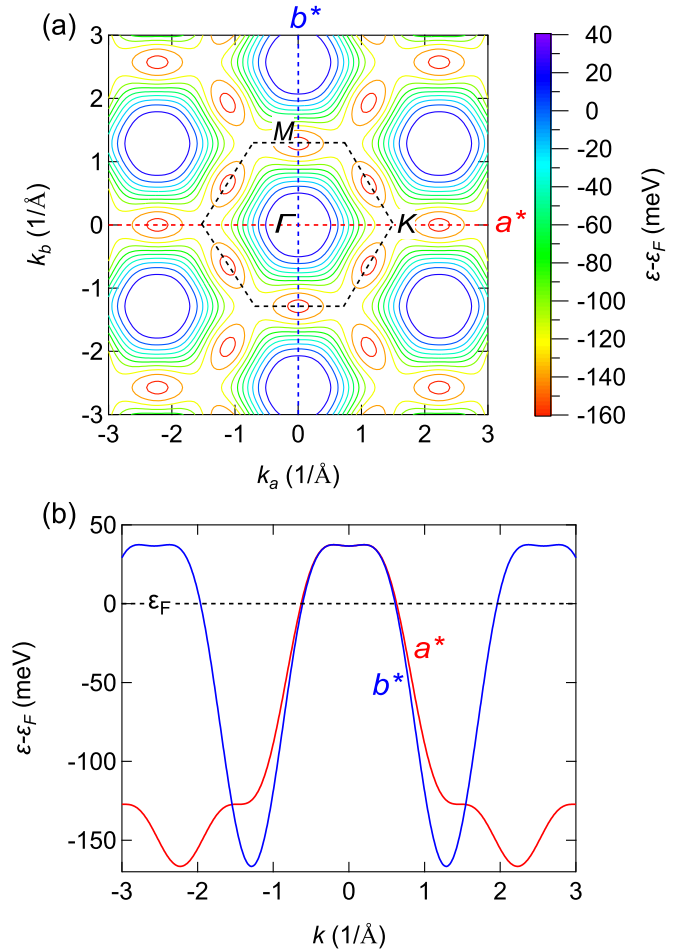


FIG. 5. (a) Constant-energy surfaces near the Fermi energy calculated by using the tight-binding model [Eq. (4)]. (b) Dispersion relations along $\Gamma \rightarrow \text{K}$ (a^* direction, red) and $\Gamma \rightarrow \text{M}$ (b^* direction, blue).

dispersions indicates a pudding mold energy band in which the thermopower is approximately determined by the difference in the velocities of electrons and holes as [9]

$$Q_i = \frac{k_B}{e} \frac{\sum (v_{i,h}^2 - v_{i,e}^2)}{\sum (v_{i,h}^2 + v_{i,e}^2)}, \quad (5)$$

where $v_{i,e}$ and $v_{i,h}$ are the velocities of electrons and holes for the i direction ($i = a, b$), respectively. Figure 6(a) presents the carrier velocity calculated as $v_a = 1/\hbar(\partial\varepsilon/\partial k_a)|_{k_b=0}$ and $v_b = 1/\hbar(\partial\varepsilon/\partial k_b)|_{k_a=0}$ as a function of energy near the Fermi energy. Although the summation in Eq. (5) is taken over all the \mathbf{k} states within the thermal energy $k_B T$, for simplicity we only consider these v_a and v_b , which largely contribute to the transport coefficients for each direction. In this approximation, one obtains $v_{i,e} = v_i(\varepsilon > \varepsilon_F)$ and $v_{i,h} = v_i(\varepsilon < \varepsilon_F)$. Figure 6(b) depicts a velocity ratio $x_i \equiv (v_{i,h}^2 - v_{i,e}^2)/(v_{i,h}^2 + v_{i,e}^2)$ for each direction as a function of the energy from the Fermi energy in magnitude. In the present energy range, which is comparable to the thermal energy $k_B T$, $x_b > x_a$ holds, leading to $Q_b > Q_a$. This is consistent with the present result shown in Fig. 3(c), indicating a validity of an itinerant picture based on the observed Fermi surface.

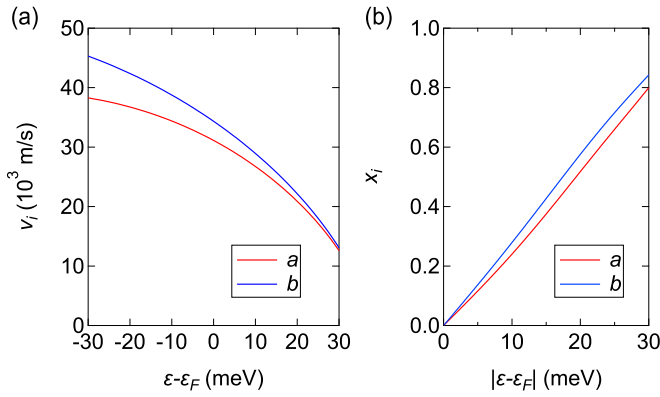


FIG. 6. (a) Electronic velocity $v_i = 1/\hbar(\partial\epsilon/\partial k_i)$ as a function of energy measured from the Fermi energy for a (red) and b (blue) directions. The velocity v_a (v_b) is calculated for $k_b = 0$ ($k_a = 0$). (b) A velocity ratio $x_i \equiv (v_{i,h}^2 - v_{i,e}^2)/(v_{i,h}^2 + v_{i,e}^2)$ for a (red) and b (blue) directions as a function of the energy measured from ϵ_F in magnitude.

We mention the anisotropy in the SDW phase below 30 K. This material shows the SDW transition at $T_{\text{SDW}} \simeq 30$ K and its onset temperature is $T_{\text{SDW}}^{\text{ON}} \simeq 100$ K. As shown in Fig. 4(a), although no prominent feature is found at $T_{\text{SDW}}^{\text{ON}}$, we observed a cusp near T_{SDW} in the temperature dependence of the thermopower anisotropy. The cusp structure in the thermopower anisotropy indicates that the electronic structure is drastically varied at T_{SDW} , as is seen in the significant change in thermopower anisotropy at the SDW transition in Fe-based superconductors [52]. On the other hand, the conductivity

anisotropy σ_b/σ_a is monotonically increased as temperature decreases, and shows no anomaly at T_{SDW} as seen in Fig. 4(b). This result implies that, although the anisotropy of the velocities is crucial since $v_b > v_a$ leads to $\sigma_b > \sigma_a$ from $\sigma_i \sim \sum (v_{i,h}^2 + v_{i,e}^2)\tau$ (where τ is the relaxation time), the conductivity anisotropy may be governed by the relaxation time, which is canceled out in the thermopower formula of Eq. (5).

IV. SUMMARY

To summarize, we have measured the anisotropies of the resistivity and the thermopower in layered $[\text{Ca}_2\text{CoO}_3]_{0.62}[\text{CoO}_2]$ and found considerable temperature variations. In high-temperature range, the anisotropy in the thermopower becomes close to unity, indicating a localized picture. On the other hand, low-temperature anisotropies are qualitatively explained in the itinerant band picture based on the results from ARPES, and the change in the electronic structure associated with the SDW transition is probed as a cusp behavior of the thermopower anisotropy. These results show a crossover from low-temperature itinerant to high-temperature localized electronic states in this material.

ACKNOWLEDGMENTS

The authors would like to thank S. Makino for an early stage of the present study. We are grateful to S. Yoshioka for allowing us to use the scanning electron microscope (SEM). We thank H. Yaguchi for discussion, and H. Utagawa and H. Hatada for experimental supports. This work was supported by JSPS KAKENHI Grants No. JP17H06136, No. JP18K03503, and No. JP18K13504.

- [1] F. Schipper, E. M. Erickson, C. Erk, J.-Y. Shin, F. F. Chesneau, and D. Aurbach, *J. Electrochem. Soc.* **164**, A6220 (2017).
- [2] I. Terasaki, Y. Sasago, and K. Uchinokura, *Phys. Rev. B* **56**, R12685(R) (1997).
- [3] G. J. Snyder and E. S. Toberer, *Nat. Mater.* **7**, 105 (2008).
- [4] K. Koumoto, Y. Wang, R. Zhang, A. Kosuga, and R. Funahashi, *Annu. Rev. Mater. Research* **40**, 363 (2010).
- [5] S. Hébert, D. Berthebaud, R. Daou, Y. Bréard, D. Pelloquin, E. Guilmeau, F. Gascoin, O. Lebedev, and A. Maignan, *J. Phys.: Condens. Matter* **28**, 013001 (2016).
- [6] W. Koshibae, K. Tsutsui, and S. Maekawa, *Phys. Rev. B* **62**, 6869 (2000).
- [7] Y. Wang, N. S. Rogado, R. J. Cava, and N. P. Ong, *Nature* **423**, 22 (2003).
- [8] H. Takahashi, S. Ishiwata, R. Okazaki, Y. Yasui, and I. Terasaki, *Phys. Rev. B* **98**, 024405 (2018).
- [9] K. Kuroki and R. Arita, *J. Phys. Soc. Jpn.* **76**, 083707 (2007).
- [10] H.-B. Yang, S.-C. Wang, A. K. P. Sekharan, H. Matsui, S. Souma, T. Sato, T. Takahashi, T. Takeuchi, J. C. Campuzano, R. Jin, B. C. Sales, D. Mandrus, Z. Wang, and H. Ding, *Phys. Rev. Lett.* **92**, 246403 (2004).
- [11] H.-B. Yang, Z.-H. Pan, A. K. P. Sekharan, T. Sato, S. Souma, T. Takahashi, R. Jin, B. C. Sales, D. Mandrus, A. V. Fedorov, Z. Wang, and H. Ding, *Phys. Rev. Lett.* **95**, 146401 (2005).
- [12] D. Qian, L. Wray, D. Hsieh, D. Wu, J. L. Luo, N. L. Wang, A. Kuprin, A. Fedorov, R. J. Cava, L. Viciu, and M. Z. Hasan, *Phys. Rev. Lett.* **96**, 046407 (2006).
- [13] J. Geck, S. V. Borisenko, H. Berger, H. Eschrig, J. Fink, M. Knupfer, K. Koepernik, A. Koitzsch, A. A. Kordyuk, V. B. Zabolotnyy, and B. Büchner, *Phys. Rev. Lett.* **99**, 046403 (2007).
- [14] T. Arakane, T. Sato, T. Takahashi, T. Fujii, and A. Asamitsu, *New J. Phys.* **13**, 043021 (2011).
- [15] N. Hamada, T. Imai, and H. Funashima, *J. Phys.: Condens. Matter* **19**, 365221 (2007).
- [16] S.-D. Chen, Y. He, A. Zong, Y. Zhang, M. Hashimoto, B.-B. Zhang, S.-H. Yao, Y.-B. Chen, J. Zhou, Y.-F. Chen, S.-K. Mo, Z. Hussain, D. Lu, and Z.-X. Shen, *Phys. Rev. B* **96**, 081109(R) (2017).
- [17] R. Funahashi, I. Matsubara, H. Ikuta, T. Takeuchi, U. Mizutani, and S. Sodeoka, *J. Appl. Phys.* **39**, L1127 (2000).
- [18] A. C. Masset, C. Michel, A. Maignan, M. Hervieu, O. Toulemonde, F. Studer, B. Raveau, and J. Hejtmanek, *Phys. Rev. B* **62**, 166 (2000).
- [19] Y. Miyazaki, M. Onoda, T. Oku, M. Kikuchi, Y. Ishii, Y. Ono, Y. Morii, and T. Kajitani, *J. Phys. Soc. Jpn.* **71**, 491 (2002).
- [20] E. Dagotto, *Science* **309**, 257 (2005).
- [21] K. Momma and F. Izumi, *J. Appl. Crystallogr.* **44**, 1272 (2011).

- [22] J. Sugiyama, H. Itahara, T. Tani, J. H. Brewer, and E. J. Ansaldo, *Phys. Rev. B* **66**, 134413 (2002).
- [23] J. Sugiyama, J. H. Brewer, E. J. Ansaldo, H. Itahara, K. Dohmae, Y. Seno, C. Xia, and T. Tani, *Phys. Rev. B* **68**, 134423 (2003).
- [24] N. Murashige, F. Takei, K. Saito, and R. Okazaki, *Phys. Rev. B* **96**, 035126 (2017).
- [25] A. Ahad, K. Gautam, K. Dey, S. S. Majid, F. Rahman, S. K. Sharma, J. A. H. Coaquira, Ivan da Silva, E. Welter, and D. K. Shukla, *Phys. Rev. B* **102**, 094428 (2020).
- [26] M. Mikami, K. Chong, Y. Miyazaki, T. Kajitani, T. Inoue, S. Sodeoka, and R. Funahashi, *J. Appl. Phys.* **45**, 4131 (2006).
- [27] P. Limelette, S. Hébert, V. Hardy, R. Frésard, C. Simon, and A. Maignan, *Phys. Rev. Lett.* **97**, 046601 (2006).
- [28] R. F. Klie, Q. Qiao, T. Paulauskas, A. Gulec, A. Rebola, S. Ögüt, M. P. Prange, J. C. Idrobo, S. T. Pantelides, S. Kolesnik, B. Dabrowski, M. Ozdemir, C. Boyraz, D. Mazumdar, and A. Gupta, *Phys. Rev. Lett.* **108**, 196601 (2012).
- [29] A. Ahad, K. Gautam, S. S. Majid, S. Francoual, F. Rahman, F. M. F. De Groot, and D. K. Shukla, *Phys. Rev. B* **101**, 220202(R) (2020).
- [30] G. D. Tang, H. H. Guo, T. Yang, D. W. Zhang, X. N. Xu, L. Y. Wang, Z. H. Wang, H. H. Wen, Z. D. Zhang, and Y. W. Du, *Appl. Phys. Lett.* **98**, 202109 (2011).
- [31] T. Takeuchi, T. Kondo, T. Kitao, K. Soda, M. Shikano, R. Funahashi, M. Mikami, and U. Mizutani, *J. Electron Spectrosc. Relat. Phenom.* **144–147**, 849 (2005).
- [32] S. Lemal, J. Varignon, D. I. Bilc, and P. Ghosez, *Phys. Rev. B* **95**, 075205 (2017).
- [33] Y. Ikeda, K. Saito, and R. Okazaki, *J. Appl. Phys.* **119**, 225105 (2016).
- [34] C. A. M. dos Santos, A. de Campos, M. S. da Luz, B. D. White, J. J. Neumeier, B. S. de Lima, and C. Y. Shigue, *J. Appl. Phys.* **110**, 083703 (2011).
- [35] M. A. Tanatar, N. Ni, G. D. Samolyuk, S. L. Budko, P. C. Canfield, and R. Prozorov, *Phys. Rev. B* **79**, 134528 (2009).
- [36] A. Bhaskar, Z.-R. Lin, and C.-J. Liu, *J. Mater. Sci.* **49**, 1359 (2014).
- [37] Y.-C. Hsieh, R. Okazaki, H. Taniguchi, and I. Terasaki, *J. Phys. Soc. Jpn.* **83**, 054710 (2014).
- [38] P. Limelette, W. Saulquin, H. Muguerra, and D. Grebille, *Phys. Rev. B* **81**, 115113 (2010).
- [39] T. Wu, T. A. Tyson, H. Chen, J. Bai, H. Wang, and C. Jaye, *J. Phys.: Condens. Matter* **24**, 455602 (2012).
- [40] J. Hejtmánek, Z. Jiráček, and J. Šebek, *Phys. Rev. B* **92**, 125106 (2015).
- [41] M. Shikano and R. Funahashi, *Appl. Phys. Lett.* **82**, 1851 (2003).
- [42] A. F. Ioffe and A. R. Regel, *Prog. Semicond.* **4**, 237 (1960).
- [43] M. Gurvitch, *Phys. Rev. B* **24**, 7404 (1981).
- [44] N. E. Hussey, K. Takenaka, and H. Takagi, *Philos. Mag.* **84**, 27 (2004).
- [45] T. Fujii, I. Terasaki, T. Watanabe, and A. Matsuda, *Jpn. J. Appl. Phys.* **41**, L783 (2002).
- [46] R. Asahi, J. Sugiyama, and T. Tani, *Phys. Rev. B* **66**, 155103 (2002).
- [47] J. Soret and M.-B. Lepetit, *Phys. Rev. B* **85**, 165145 (2012).
- [48] A. Rébola, R. Klie, P. Zapol, and S. Ögüt, *Phys. Rev. B* **85**, 155132 (2012).
- [49] B. Amin, U. Eckern, and U. Schwingenschlögl, *Appl. Phys. Lett.* **110**, 233505 (2017).
- [50] B. J. Powell, *arXiv:0906.1640*.
- [51] Although the crystal system of $[\text{Ca}_2\text{CoO}_3]_{0.62}[\text{CoO}_2]$ is monoclinic, the angle $\beta \sim 98^\circ$ is close to 90° . We then assume that the a^* direction is close to the a direction.
- [52] M. Matusiak, M. Babij, and T. Wolf, *Phys. Rev. B* **97**, 100506(R) (2018).